Biointerface Research in Applied Chemistry
Open-Access Journal (ISSN: 2069-5837)

*Review*
**Volume 14, Issue 5, 2024, 120**
https://doi.org/10.33263/BRIAC145.120

# Imaging Non-Small Cell Lung Cancer EGFR Del19 and L858R with Radiolabeled Small Molecule

**Muammar Fawwaz [1,*], Mamat Pratama [1], Masdiana Tahir [1], Emil Salim [2], Nurul Dwi Wulandari [1], Saparuddin Latu [3], Muzakkir Baits [1]**

1. Laboratory of Pharmaceutical Chemistry, Faculty of Pharmacy, Universitas Muslim Indonesia, Makassar, Indonesia
2. Faculty of Pharmacy, Universitas Sumatera Utara, Medan, Indonesia
3. Department of Pharmacy, Faculty of Pharmacy, Universitas Megarezky, Makassar, Indonesia

* Correspondence: muammar.fawwaz@umi.ac.id (M.F.);

Scopus Author ID 56085116100

**Received: 16.09.2023; Accepted: 28.01.2024; Published: 21.07.2024**

**Abstract:** Non-small cell Lung Cancer (NSCLC) is the leading cause of cancer death, with approximately 1.3 million deaths annually worldwide. Tyrosine Kinase Inhibitors (TKIs) targeting the Epidermal Growth Factor Receptor (EGFR) are used as therapy for NSCLC patients. However, patients receiving first and second-generation TKIs will usually develop drug resistance within 6-12 months after treatment. Resistance occurs because of EGFR mutations that interfere with the therapeutic process. Therefore, detecting the type of EGFR mutation before treatment by TKIs is necessary. Molecular imaging techniques such as Positron Emission Tomography (PET) and Single Photon Emission Computed Tomography (SPECT) promise non-invasive techniques for mutation detection. This study aims to review articles on radiotracers developed to detect common EGFR mutations, such as exon 19-del and exon 21 L858R mutation in NSCLC. The method used in this research is to search for articles through international databases such as Scopus, SciFinder, and PubMed with inclusion and exclusion parameters. The results showed that several radiotracers were selective for EGFR 19-del and L858R. However, some compounds need to be modified structurally to have high specificity.

**Keywords:** Del19; L747-A750; L858R; PET; radiotracer; SPECT.



## 1. Introduction

Lung cancer is the most common type of cancer in both men and women, which ranks first in the number of cancer deaths in the US in 2023, at 21% for both sexes [1]. Non-small cell lung cancer (NSCLC) is the most common type of lung cancer [1,2]. The epidermal growth factor receptor (EGFR) therapy, such as tyrosine kinase inhibitors (TKIs), exhibited effective response by NSCLC patients [3,4]. However, sequencing of the EGFR gene revealed that most tumors that respond to EGFR TKIs harbor activating mutations in the EGFR kinase domain [5,6]. The most common mutations in EGFR are in exon 19 (Del19), which eliminates amino acids 747–750 (Leu-Arg-Glu-Ala), and in exon 21, where there is an L858R amino acid substitution [7-9]. Therefore, the discovery of a new generation of TKIs continues to be pursued through structural modifications to overcome resistance to TKIs due to EGFR mutations.

Determining the type of mutation in NSCLC patients prior to therapy is necessary for effective therapy. Imaging agents resulting from TKIs radiolabeling are promising in determining the type of mutation in NSCLC [10,11]. Radiolabeling is carried out using

positron-emitting radionuclides, which can then be used as tumor imaging agents through modulating positron emission tomography (PET) and single photon emission computed tomography (SPECT) [12-14]. The use of radiotracer in cancer diagnostic techniques, also known as nuclear medicine imaging, is a revolutionary, highly effective, non-invasive approach for patients that aims to differentiate the types of mutations in EGFR [15-17].

This diagnostic technique complements some of the limitations of the most commonly used biopsy technique. Some of the limitations of a biopsy include its inability to describe the overall condition of the tumor due to the small number of samples taken while the nature of the cancer is very heterogeneous [18-20]. In addition, repeated sampling of the biopsy method is invasive in patients [21-23]. Thus, nuclear medicine imaging plays a very important role in making a diagnosis, which, of course, has a direct positive implication in increasing the effectiveness of therapy for NSCLC patients.

Several types of radiotracers have been developed to detect mutations in the EGFR. These radiotracers not only focus on the EGFR Del19 and L858R mutations but also several radiotracers focus on the double EGFR L858R/T790M mutation [16,24,25]. Nonetheless, this study will focus on the active mutant EGFR Del19 and L858R. Some active mutant radiotracers still have limitations to be used optimally as imaging agents. Therefore, this study aims to record several radiotracers that have been developed to diagnose mutations in EGFR Del19 and L858R.

Here, we found that several radiotracers have been developed with either PET or SPECT modulation. The radiotracer was fundamentally tested on the NSCLC cell line, such as on the EGFR Del19, L858R mutations, L858R/T790M mutation, and EGFR WT both in vitro and in vivo evaluation.

## 2. Radiotracer targeting EGFR Del19 and L858R

To successfully use EGFR-TKIs on patients with NSCLC who have EGFR Del19 and L858R mutations, PET or SPECT imaging might be a valuable and non-invasive approach for identifying patients sensitive to EGFR-TKIs. The fundamental evaluation of numerous radiotracers was performed on several target cell lines, as indicated in Table 1, to distinguish the preferential accumulation of the radiotracer in NSCLC. Table 2 and Figure 1 show certain radiolabeled targeting EGFR Del19 and L858R mutations.

**Table 1.** Cell lines in the radiotracer evaluation targeted EGFR Del19 and L858R mutations.

| No. | EGFR Over-expression | Cell lines |
|---|---|---|
| 1. | L858R | H3255 |
| 2. | Del19 | H1650, PC9, HCC827 |
| 3. | L858R/T790M | H1975 |
| 4. | WT | H441, H358, PC14, A549, A431 |
| 5. | WT transfected | H1299 |
| 6. | Low EGFR expression | H520 |

**Table 2.** Radiolabeled small molecules for imaging EGFR Del19 and L858R mutations.

| No | Radiotracer | Targeted EGFR | Cell preference | Cell uptake | Tumor accumulation |
|---|---|---|---|---|---|
| 1. | [$^{18}$F]PEG6-IPQA [21] | L858R | H3255 | 400 cell/medium ratio | 2.34 ± 0.13% ID/g (2 hours) |
| 2. | [$^{131/124}$I]morpholino-IPQA [26] | L858R | EGFR-transfected H1299 | 3.12 ± 0.304 cell/medium ratio | 0.280 ± 0.000 % ID/g (1 hour), 0.251 ± 0.001 (4 hours) |
| 3. | [$^{125}$I]PHY [27] | L858R | H3255 | - | 2.04%ID/g (1 hour) |
| 4. | [$^{11}$C]erlotinib [28] | Del19 | HCC827 | - | 3.2 ± 0.3%ID/g (25 minutes) |
| 5. | [$^{18}$F]afatinib [28] | Del19 | HCC827 | - | 1.2 ± 0.2%ID/g (10 minutes) |
| 6. | [$^{11}$C]PD153035 [29] | Del19 | HCC827 | 5.365 ± 0.246 cell count | > 2500 cell count (40 minutes) |

| No | Radiotracer | Targeted EGFR | Cell preference | Cell uptake | Tumor accumulation |
|---|---|---|---|---|---|
| 7. | [$^{18}$F]IRS [30] | Del19 | HCC827 | 19.07 ± 0.70% | 1.90 ± 0.31%ID/g (30 minutes) |
| 8. | [$^{99m}$Tc]HYNIC-MPG [31] | Del19 | PC9 | 4.89 ± 0.08% | 6.16 ± 0.28% (2 hours) |
| 9. | [$^{18}$F]APP-1 [32] | L858R | H3255 | 46.8 ± 7.6% dose/mg protein | 3.62%ID/g (1 hour) 3.80%ID/g (3 hours) |
| 10. | [$^{18}$F]FTP2 [10] | L858R | H3255 | 32.5 ± 2.0% ID/mg protein | 2.5 ± 0.3%ID/g (3 hours) |
| 11. | [$^{18}$F]MPG [33] | Del19 | HCC827 | > 4% of total radioactivity | 7.22 ± 0.28%ID/g (1 hour) |
| 12. | 6-O-[$^{18}$F]FEE [34] | Del19 | HCC827 | - | 1 SUV (1 hour) |
| 13. | methylindole-[$^{11}$C] osimertinib [35] | Del19 | HCC827 | - | 2.17 ± 0.27 %ID/g (45 minutes) |
| 14. | dimethylamine-[$^{11}$C] osimertinib [35] | Del19 | HCC827 | - | 2.16 ± 0.14 %ID/g (45 minutes) |

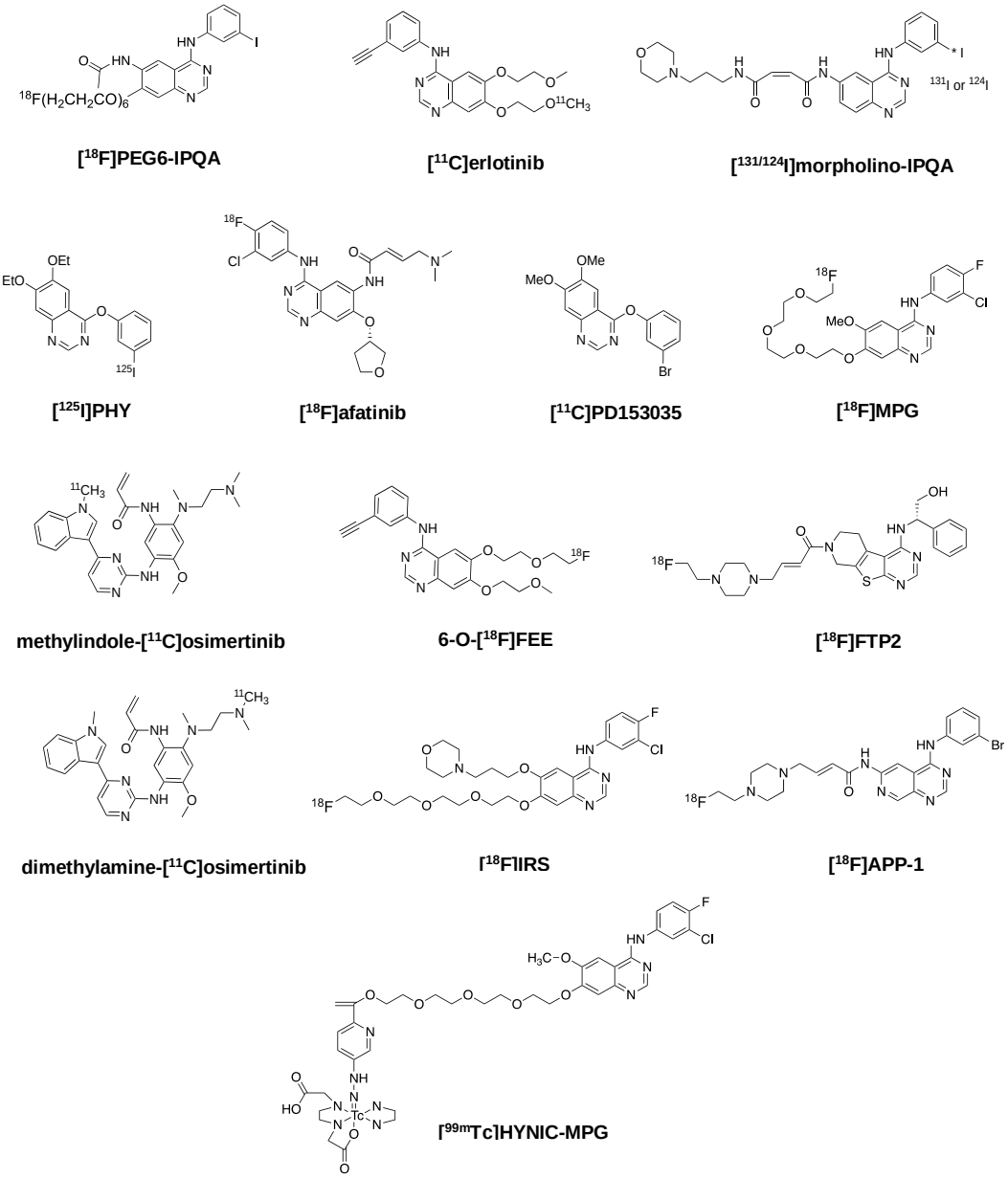


**Figure 1.** Radiotracer for imaging EGFR Del19 and L858R mutations.

*2.1. [$^{18}$F]PEG6-IPQA.*

All four cell lines showed rapid uptake of 4-[(3-iodophenyl)amino]-7-{2-[2-{2-(2-[2-{2-([$^{18}$F] fluoroethoxy)- ethoxy}- ethoxy]-ethoxy)- ethoxy}-ethoxy]- quinazoline-6-yl

acrylamide ([$^{18}$F]PEG6-IPQA) during the initial phase (first 20 min). After that, [$^{18}$F]PEG6-IPQA accumulation reached a plateau in H441, H1975, and PC14 cells at around 30–40 cells/medium concentration ratio. In contrast, in H3255 cells, radiotracer accumulation continued to increase for up to 1 hour and reached a plateau at a cell-to-medium concentration ratio of 400–600. The magnitude of [$^{18}$F]PEG6-IPQA accumulation in H3255 cells was more than 10-fold higher than in H441 cells. Radiotracer uptake studies demonstrated significant retention of [$^{18}$F]PEG6-IPQA in H3255 cells (cells per media concentration ratio of approx. 400), which accounted for 65% of the total accumulated radioactivity between 60 and 120 min of incubation. In contrast, almost 50% of [$^{18}$F]PEG6-IPQA radioactivity was washable from H441 cells, more than 60% from PC14 cells, and more than 70% from H1975 cells. After the washout of PC14 and H1975 cells, the magnitude of [$^{18}$F]PEG6-IPQA retention was less than 10 cells/medium concentration ratio. The magnitude of [$^{18}$F]PEG6-IPQA accumulation in all tested cell lines decreased significantly in the presence of gefitinib (Iressa®, 100 μM/L) in culture medium [21].

PET with computed tomography (CT) imaging showed a greater accumulation of [$^{18}$F]PEG6-IPQA in the H3255 tumor (2.34 ± 0.13% ID/g) than in other tumors. Radiotracer accumulation in tumors H441 (1.59 ± 0.44% ID/g), H1975 (1.05 ± 0.09% ID/g) and PC14 (0.90 ± 0.11% ID/g). This suggests [$^{18}$F]PEG6-IPQA binds specifically to the EGFR L858R mutation [21].

In an in vivo blocking study, [$^{18}$F]PEG6-IPQA against tumors with the addition of gefitinib as an inhibitor caused the accumulation of H3255 in tumors to decrease by 50% to 1.38 ± 0.43% ID/g. This suggests that gefitinib significantly inhibited [$^{18}$F]PEG6-IPQA accumulation against H3255 cells. Meanwhile, the accumulation of radiotracer in H441 tumors, which are EGFR WT, did not decrease significantly (1.58 ± 0.43% ID/g) after pretreatment with gefitinib. Based on these data, it can be concluded that [$^{18}$F]PEG6-IPQA has a high sensitivity to H3255, which is EGFR L858R [21].

Quantitative autoradiography (QAR) demonstrated a preference for accumulation of [$^{18}$F]PEG6-IPQA in an adequate portion of H3255 tumor xenografts (3.01 ± 0.84% ID/g). In contrast, no specific accumulation of [$^{18}$F]PEG6-IPQA was observed in necrotic tumor areas. Radiotracer accumulation in H441 tumors (2.53 ± 0.15% ID/g) was lower than in H3255 xenografts, whereas in H1975 tumors (1.27 ± 0.12% ID/g) and PC14 (1.54 ± 0.14% ID/g), significantly lower. Pretreatment with gefitinib (Iressa®) resulted in a four-fold decrease in radiotracer accumulation in H3255 tumors (0.92 ± 0.13% ID/g; $P < 0.05$) and a three-fold decrease in H3255 tumors. H441 (0.78 ± 0.06% ID/g; $P < 0.05$). In contrast to the accumulation of radiotracer on H1975 (1.05 ± 0.01% ID/g) and PC14 (1.17 ± 0.10 ID/g), there was no significant difference in accumulation after treatment with gefitinib (Iressa®) [21].

### *2.2. [$^{131/124}$I]morpholino-IPQA.*

The accumulation of [4-(3-[$^{124}$I]iodoani-lino)-quinazolin-6-yl]-amide-(3-morpholin-4-yl-propyl)-amide ([$^{124}$I]morpholino-IPQA) at 10 min in all four types of NSCLC was fast and after that reached a plateau at 60 min. The cell-to-medium ratio (CMR) of [$^{131}$I]morpholino-IPQA in L858R (3.12 ± 0.304) was approximately 2-fold higher than that of E746-A750 (1.57 ± 0.17) and WT H1299 cells transfected (1.47 ± 0.001) [26].

Loss of [$^{131}$I]morpholino-IPQA accumulation in L858R and E746-A750 cells can be characterized by a fast washout, followed by a plateau, with a slow but slight decrease. In

contrast, H1299 cells transfected with WT EGFR showed a consistent decrease in CMR over time. Furthermore, the washout study at 120 min showed higher radiotracer retention in L858R (8.9 ± 0.2 CMR) and E746-A750 del cells (12.6 ± 3.2 CMR) than in EGFR-transfected H1299 (5.7 ± 0.4 CMR) and vector-transfected H1299 (6.6 ± 0.3 CMR) [26].

In vivo PET imaging was performed on 18 mice (6 per tumor pair) before and after treatment with gefitinib (Iressa®). Evaluation using Micro PET showed that the highest radiotracer accumulation was observed in the L858R tumor xenograft at 24 hours after administration. Accumulation in L858R cells was 1.23-, 2.36-, and 3.08-fold higher than that of E746-A750 del, WT EGFR-transfected, and vector-transfected tumor xenografts in the initial group, respectively. Pretreatment with gefitinib (Iressa®, 100 mg/kg) 1 hour before administration of [$^{124}$I]morpholino-IPQA resulted in a decrease in radiotracer accumulation in L858R and del E746-A750 tumors by 53% and 38%. In contrast, radiotracer accumulation in EGFR-transfected and WT vector-transfected tumor xenografts before and after gefitinib (Iressa®) treatment was unchanged [26].

The results of the biodistribution evaluation of [$^{131}$I]morpholino-IPQA showed high accumulation in the pancreas, kidney, stomach, lung, liver, and small and large intestines in the first hour after radiotracer injection. In contrast, blood, heart, liver, and spleen showed redistribution 24 hours after [$^{131}$I]morpholino-IPQA administration. The excretion pattern of this radiotracer is through hepatobiliary clearance followed by a rapid increase in radioactivity in the blood and subsequent renal excretion. Radiotracer accumulation in the four tumor types had peak radioactivity concentrations in the first hour and gradually decreased over time. Nonetheless, the radiotracer retention in the L858R xenograft tumor was longer than in the other tumors [26].

The tumor-to-blood (T/B) and tumor-to-muscle (T/M) ratios were not distinguishable among four tumor xenografts up to 24 hours after radiotracer injection. The T/B and T/M ratios in L858R tumor xenograft 24 hours after radiotracer injection were 2.64 and 13.89, respectively. The E746-A750 del tumor xenograft had a similar T/B and T/M ratio compared to the L858R group. The L858R tumor xenograft also had a better tumor-to-vector (T/V) ratio 24 hours after radiotracer administration than the other 2 xenografts [26].

In conclusion, an enhanced binding of [$^{131/124}$I]morpholino-IPQA derivatives to the ATP binding site of mutant kinase of L858R or E746-A750 del EGFR mutant warrants that PET imaging with [$^{124}$I]morpholino-IPQA has a potential for identification of tumors with high EGFR kinase activity in NSCLC and the monitoring or selection of individual therapies with EGFR inhibitors. Further optimization of this radio compound class would be necessary to lower lipophilicity and reduce hepatobiliary clearance [26].

### *2.3. [$^{125}$I]PHY.*

In A431-bearing mice, the biodistribution of radioiodinated 4-(3-iodo-phenoxy)-6,7-diethoxy-quinazoline ([$^{125}$I]PHY) at 1 hour post-injection revealed high accumulation in the intestine (30.6%ID/g) and moderate radiotracer accumulation in the liver (3.3%ID/g) and stomach (4.6%ID/g). Besides, there was low radioactivity uptake in other normal tissues. The radiotracer accumulation in blood, lung, and brain is low, resulting in relatively high T/B and T/L ratios. This shows that radioiodinated PHY can be used to image lung and brain cancers [27].

Although gefitinib sensitivity in A431 was 10-fold higher than in A549, and western blotting demonstrated extensive EGFR expression in A431 when compared to A548, radiotracer accumulation in A431 was only 1.5-fold more than in A549. The radiotracer accumulation at 1-hour post-injection in tumor A431 (1.56%ID/g) was similar to that of A549 (1.04%ID/g), H1650 (1.31%ID/g), H1975 (0.94%ID/g), and H3255 (2.04%ID/g). The radiotracer accumulated in some tumors due to the nonspecific binding of [$^{125}$I]PHY. The radiotracer accumulation in A431, H1650, and H3255 showed good tumor-to-lung (T/L) ratios at 1-hour post-injection [27].

They are blocking the study by an excess dose of gefitinib reduced [$^{125}$I]PHY uptake in A431 up to 52% (from 0.50%ID/g to 0.26%ID/g). Therefore, reducing nonspecific binding would allow for a more precise estimation of EGFR expression [27].

Although EGFR expression levels are insufficient to predict treatment with EGFR-TK inhibitors, EGFR overexpression in tumors is a need for EGFR-targeted therapy. Our findings imply that radioiodinated PHY is a promising imaging agent for detecting EGFR expression levels as a first screening marker, but further molecule development is required to predict gefitinib sensitivity [27] appropriately.

*2.4. [$^{11}$C]erlotinib and [$^{18}$F]afatinib.*

PET imaging was used with both tracers in all three xenograft models to see if the irreversible inhibitor improved tumor targeting. The mice were transplanted with a single tumor on the left flank to create an appropriate location for the background tissue. In this way, the animal's right flank functioned as a reference location because the contralateral tissue was identical except for the absence of tumor cells. The tumor and the background were manually delineated using an extra [$^{18}$F]FDG scan done immediately after the TKI-PET scan. As a quantitative measure of uptake, these PET scans can be used to calculate the percentage of injected dose per gram of tissue [28].

Both tracers exhibit high uptake in the liver and kidneys, which is typical for IV-administered small molecular PET tracers because these organs represent the principal excretion and catabolism routes. The most noticeable difference between the two tracers is that [$^{11}$C]erlotinib has much slower kinetics than [$^{18}$F]afatinib, regardless of the xenograft line tested [28].

Actually, [$^{11}$C]erlotinib (reversible inhibitor) reaches its maximum uptake in the tumor (HCC827) at 25 minutes of 3.2 0.3%ID/g PI, whereas [$^{18}$F]afatinib (irreversible inhibitor) activity concentration in the tumor (HCC827) is already at 1.2 0.2%ID/g at 10 minutes post-injection, indicating faster kinetics and/or clearance. Compared to [$^{18}$F]afatinib, this resulted in a greater activity concentration in all tissues of interest (tumor and background). With their distinct mutational state, the tracers appear to have a comparable uptake pattern across the numerous xenograft lines regarding general imaging features. [$^{11}$C]erlotinib does not accumulate selectively in xenografts expressing WT EGFR (A549) [28].

There was no selective absorption of either radiotracer in the double mutant xenografts (H1975) with a sensitizing mutation (L858R) and an acquired resistance mutation (T790M). This conclusion is consistent with erlotinib's effectiveness, as it has no therapeutic impact in this xenograft model. However, afatinib reduced tumor growth rate in H1975 xenografts modestly, but there was no significant tumor uptake of [$^{18}$F]afatinib [28].

[$^{11}$C]erlotinib and [$^{18}$F]afatinib exhibit the greatest absorption in HCC827 xenografts. The T/B ratio of [$^{18}$F]afatinib is slightly higher than that of [$^{11}$C]erlotinib. This study reveals

TKI-PET's capacity to effectively image TKI uptake in these tumors. In the HCC827 xenograft line, PET imaging was performed with co-injection of unlabeled afatinib (100 to 6,000 ng) with the tracer. With an additional excess dose of afatinib, the radiotracer accumulation was inhibited to the background level [28].

The [$^{11}$C]erlotinib uptake was undetected in the WT xenograft line (A549), but [$^{18}$F]afatinib uptake was minimal. This could be owing to changes in retention caused by biophysical differences between the two tracers, [$^{18}$F]afatinib's ability to bind covalently to additional targets (HER2 and ERBB4 in addition to EGFR), or differences in affinity for efflux transporters. An imaging investigation was conducted in the presence of an efflux transporter inhibitor to understand better the role of P-gp in PET tracer uptake [28].

TKI-PET tracers [$^{11}$C]erlotinib and [$^{18}$F]afatinib are helpful for imaging treatment-sensitive xenografts with EGFR exon 19 deletion mutations. The good T/B ratio could be employed in clinical decision-making for both tracers. The difference between a reversible and irreversible inhibitor could not be proven in a conventional PET imaging scenario since both tracers displayed similar tumor uptake kinetics [28].

### *2.5. [$^{11}$C]PD153035.*

The experiment used logarithmic phase cells to quantify the radiotracer version of 4-N-(3-bromoanilino)26,7-dimethoxyquinazoline ([$^{11}$C]PD153035) uptake. The [$^{11}$C]PD153035 was accumulated faster and earlier in HCC827 than the other cell lines (P = 0.05). The radioactive uptake showed an attenuation tendency, and there were substantial differences in g-cell counts at different incubation times. The [$^{11}$C]PD153035 uptake of PC9 and A549 cells was unimodal; after 25 minutes of incubation, the highest g-cell counts observed were larger in PC9 cells than in A549 cells, and the curves steadily deteriorated. The H1975 cells had the lowest [$^{11}$C]PD153035 absorption, which varied minimally depending on incubation time [29].

The blocking study used various doses of erlotinib and cetuximab that were pretreated for 2 hours before cells in each group were cultured with [$^{11}$C]PD153035 for 20 minutes. When co-incubated with erlotinib, the accumulation of [$^{11}$C]PD153035 in HCC827 and PC9 cells dropped significantly but remained unchanged when co-incubated with cetuximab. The accumulation of [$^{11}$C]PD153035 in A549 cells dropped slightly when co-incubated with various doses of erlotinib but remained unchanged when co-incubated with cetuximab. There was no significant difference in [$^{11}$C]PD153035 accumulation by H1975 cells after co-incubation with various dosages of erlotinib and cetuximab [29].

The xenograft's features on PET/CT imaging showed that HCC827 xenografts revealed radioactivity 5 minutes after injection of [$^{11}$C]PD153035, which remained reasonably high throughout the scanning process. Radioactive accumulation was lower in PC9 xenografts than in HCC827 xenografts (P = 0.05). The radioactive uptake in the A549 and H1975 xenografts was much lower than in the HCC827 xenografts [29].

### *2.6. [$^{18}$F]IRS.*

The radiotracer N- (3- chloro- 4- fluorophenyl)- 7- [2- (2- {2- [2- (fluoro-[$^{18}$F])ethoxy]ethoxy}ethoxy)ethoxy]-6-(3-morpholinopropoxy)Quinazolin-4-amine ([$^{18}$F]IRS) is a radiotracer that is produced in steps and labeled with fluor-18 radionuclide. The chemical purity of [$^{18}$F]IRS was determined by HPLC, with a radiotracer purity of greater than 98.5%. Several assays were then performed to determine the activity of [$^{18}$F]IRS on target cells [30].

Cell uptake and efflux assays were performed on four NSCLC cells: HCC827, H1975, H358, and H520. HCC827 cells accumulated substantially more [$^{18}$F]IRS than the other three cells. The maximum uptake of [$^{18}$F]IRS in HCC827 cells was reported two hours after incubation, reaching 19.07±0.70%. Even two hours after incubation, the accumulation of [$^{18}$F]IRS remained at 4.10 ± 1.06% of the total radioactivity input, which was much larger than the other three cells in the efflux research. According to the findings of the two experiments, [$^{18}$F]IRS binds selectively to EGFR L858R [30].

The biodistribution evaluation showed that the highest level of radiotracer [$^{18}$F]IRS in the liver after 30 minutes was 2.12 ± 0.60%ID/g. The accumulation of radiotracer in the kidney reached the greatest value of 6.86 ± 2.81%ID/g, indicating that most of the [$^{18}$F]IRS radiotracer is eliminated in the urine. Meanwhile, the accumulation of [$^{18}$F]IRS radiotracer in the lungs after 30 minutes was only 1.90 ± 0.31%ID/g. In this scenario, the accumulation is beneficial for PET/CT imaging in NSCLC since it does not interfere with viewing the lung area. According to the research findings, [$^{18}$F]IRS is highly selective for EGFR-TKI, particularly EGFR L858R [30].

*2.7. [$^{99m}$Tc]HYNIC-MPG.*

The 2-{2-(2-[2-{4-(3-chloro-4- fluorophenylamino)- 6-methoxyquinazolin-7-yloxy}ethoxy]ethoxy)ethoxy} ethyl-6-hydrazinylnicotinate hydrochloride ([$^{99m}$Tc]HYNIC-MPG) cell uptake and efflux study was performed on four NSCLC cells that differed in their EGFR overexpression. Accumulation in PC9 cells was the highest of all cells. The maximum accumulation of [$^{99m}$Tc]HYNIC-MPG in PC9 cells was seen two hours after incubation, reaching 22.73 ± 1.63%. The addition of PD153035 prevented the accumulation of [$^{99m}$Tc]HYNIC-MPG in PC9 cells, and the uptake of [$^{99m}$Tc]HYNIC-MPG dropped from 22.73 ± 1.63% to 4.89 ± 0.08%, with no change in the other three NSCLC cells. This implies that [$^{99m}$Tc]HYNIC-MPG selectively binds to the EGFR exon 19 deletion mutant. [$^{99m}$Tc]HYNIC-MPG retained well in PC9 cells at 6.16 ± 0.28% after two hours of incubation in cell efflux, which was significantly higher than in cells H1975, H358, and H520. This shows that [$^{99m}$Tc]HYNIC-MPG can be utilized to track EGFR mutation status processes at the cellular level throughout time [31].

The radiotracer accumulated highest in PC9 cells at 2 h after injection compared to H1975, H358, and H520 cells in the *ex vivo* biodistribution experiment. This is consistent with SPECT imaging, which demonstrates clear visualization of PC9 cells. The liver has the highest accumulation of [$^{99m}$Tc]HYNIC-MPG since it is the body's primary metabolism site. Meanwhile, [$^{99m}$Tc]HYNIC-MPG accumulation in the brain was very low for all cancers, showing that [$^{99m}$Tc]HYNIC-MPG did not cross the blood-brain barrier [31].

Based on the findings, it is reasonable to conclude that the selectivity of [$^{99m}$Tc]HYNIC-MPG is considerably higher in PC9 cells, implying that [$^{99m}$Tc]HYNIC-MPG can be utilized to identify NSCLC tumors with high EGFR L858R potential [31].

*2.8. [$^{18}$F]APP-1.*

Cell uptake study of [$^{18}$F]APP-1 on two NSCLC cells (H3255 and H1975) showed that the radiotracer uptake in H3255 cells was 2-fold higher than that of H1975 cells. Blocking study with the addition of Osimertinib exhibited that the uptake of H3255 cells reduced from 104±8.6% dose/mg protein to 46.8±7.6% dose/mg protein, while the uptake of H1975 cells

remained consistent. These findings suggest that [$^{18}$F]APP-1 can bind selectively to the EGFR L858R mutation [32].

The biodistribution of [$^{18}$F]APP-1 in H3255 tumor carrier rats revealed that the intestine accumulated the most, with the small intestine accumulating 44.94% ID/g 1 hour after injection and the large intestine accumulating 59.65% ID/g 3 hours after injection and excreted over time. The radiotracer accumulation in bone was low. As a result, [$^{18}$F]APP-1 was stable in vivo. The accumulation of [$^{18}$F]APP-1 in tumors remained at least 3 hours (3.62% ID/g at 1 hour, 3.80% ID/g at 3 hours) [32].

In vivo blocking study using AZD9291 effectively reduced [$^{18}$F]APP-1 accumulation in H3255 tumors (54% reduction) at 3 h post-injection. In contrast, excess AZD9291 did not prevent accumulation in H1975 tumors. These findings are consistent with the cell uptake studies. These findings demonstrate that [$^{18}$F]APP-1 binds selectively to L858R mutant EGFR-TK but not to L858R/ T790M mutant EGFR-TK in mice with mutant-EGFR-TK tumors [32].

PET imaging with the radiotracer [$^{18}$F]APP-1 on mice with H3255 and H1975 tumors. The visualization findings obtained on H3255 tumors were clearer than those obtained on H1975 after 3 hours of radiotracer administration. In addition, after picture acquisition, we evaluated the radioactivity in each organ and tissue and estimated the tumor-to-tissue (T/T) ratio. The radioactivity ratio in H3255, T/B (3.12), T/M (6.80), and T/L (3.25) is much better than the radioactivity ratio in H1975; T/B (0.74), T/M (2.95) and T/L (0.74). These findings suggest that [$^{18}$F]APP-1 can be used as an imaging probe to target the L858R mutant EGFR [32].

### *2.9. [$^{18}$F]FTP2.*

The [$^{18}$F]FTP2 cell uptake was evaluated using two NSCLC cells, H3255 and H1975. The [$^{18}$F]FTP2 uptake in H3255 cells was 32.5 ± 2.0% ID/mg protein. Radiotracer accumulation in H3255 cells is almost 3-fold higher than that of H1975 cells, with only 9.51 ± 0.6% ID/mg protein. In vitro blocking assays using excess dose of gefitinib revealed that radiotracer accumulation was reduced by 50% in H3225 cells but not in H1975 cells. This suggests that [$^{18}$F]FTP2 binds specifically to EGFR L858R and not EGFR L858R/T790M against H3255 cells [10].

The [$^{18}$F]FTP2 biodistribution test in rats revealed that [$^{18}$F]FTP2 accumulation reached 2.5 ± 0.3% ID/g in H3225 cells but only 0.9 ± 0.1% ID/g in H1975 cells, which was 2.7 times lower than in H3225 cells. Because FTP2 has a hydrophobic structure, it accumulates in tissues other than tumor cells. The addition of gefitinib as an inhibitor reduced [$^{18}$F]FTP2 accumulation in H3225 cells by 37% but not in H1975 cells. These results are consistent with those of the in vitro uptake study [10].

The visualization results of PET imaging on H3225 cells were clearer than those on H1975 cells. These findings corroborate previous research on cell uptake and inhibition with gefitinib, implying that the radiotracer [$^{18}$F]FTP2 binds with high affinity and is selective for EGFR with the L858R mutation [10].

### *2.10. [$^{18}$F]MPG.*

The polyethylene glycol (PEG)–modified (PEGylated) anilinoquinazoline derivative, [2-{ 2-( 2- [2-{ 4-( 3- chloro- 4- fluorophenylamino) -6- methoxyquinazolin- 7-

yl}oxy]ethoxy)ethoxy}ethoxy]ethyl 4-methylbenzenesulfonate (T-MPG) was labeled with [$^{18}$F]F using a simple one-step method to generate the [$^{18}$F]MPG radiotracer [33].

The radiotracer uptake experiment revealed that HCC827 cells had much higher cell uptake than H1975, H520, and H358 cells. Furthermore, HCC827 cells treated with gefitinib accumulated 90% less 18F-MPG than cells not treated with gefitinib. [$^{18}$F]MPG and gefitinib compete for binding to the cell's EGFR receptor. This demonstrates that [$^{18}$F]MPG inhibits EGFR E746-A750del more selectively than EGFR L858R/T790M and EGFR WT [33].

PET imaging revealed that HCC827 tumors accumulated more [$^{18}$F]MPG than H1975, H520, or H358 cells. The maximum accumulation of [$^{18}$F]MPG in HCC827 tumors was 7.22 ± 0.28% ID/g, whereas tumors H1975, H520, and H358 had significantly lower accumulations of 3.93 ± 0.44% ID/g, 3.59 ± 0.93% ID/g, and 4.11 ± 0.46% ID/g, respectively [33].

The effective dose of [$^{18}$F]MPG radiotracer for humans is predicted to be around 6.3 ± 2.27 Sv/MBq, which is comparable to the effective dose of other 18F-labeled diagnostic radiotracers, such as 19.0 Sv/MBq for [$^{18}$F]FDG. As a result, the use of the [$^{18}$F]MPG radiotracer as a tracer in PET imaging for humans is deemed safe [33].

Several [$^{18}$F]MPG selectivity assays revealed that the compound was selective for HCC827 tumors (EGFR E746-A750del). [$^{18}$F]MPG PET/CT is a promising non-invasive approach for identifying patients who are responsive to EGFR-TKI therapy and monitoring its efficacy [33].

*2.11. 6-O-[$^{18}$F]FEE.*

The kinetics of radioactivity distribution in NSCLC tumor-bearing mice were studied for 1 hour after intravenous injection of 6-O-[$^{18}$F]FEE. TACs show two to threefold higher radioactivity concentrations in HCC827 tumors than NCI-H1975 and QG56 tumors, with mean SUVs of 1.0, 0.5, and 0.3 after 60 minutes after injection. Furthermore, radioactivity was preserved in HCC827 and NCI-H1975 tumors after initial accumulation, but QG56 tumors showed a steady reduction in radioactivity concentration [34].

To determine if the accumulation of radioactivity in HCC827 and NCI-H1975 tumors was selective, tumor-bearing mice were given erlotinib in excess (6.4 0.4 mg/kg) 3-10 minutes before 6-O-[$^{18}$F]FEE injection. Although the difference was not statistically significant, pre-administration of erlotinib resulted in a nearly twofold reduction in HCC827 tumor uptake after 60 minutes following 6-O-[$^{18}$F]FEE injection (mean SUVs of 1.04 and 0.55). In contrast, radioactivity concentrations in NCI-H1975 tumors increased following erlotinib pre-injection, from 0.5 to 0.7 at 60 minutes after 6-O-[$^{18}$F]FEE injection [34].

The primary route of 6-O-[$^{18}$F]FEE elimination was hepatobiliary clearance. The metabolic fate of 6-O-[$^{18}$F]FEE was investigated 2, 15, and 30 minutes after injection into BALB/c mice. To that purpose, mice were slaughtered at the designated periods following injection, after which blood and urine samples were collected, and the entire liver was excised. The percentages of extracted radioactivity from the blood and liver at each time point revealed constant levels of 49 ± 14% and 84 ± 2% extraction from the blood and liver, respectively, for the three examined time points [34].

The radiotracer has potency and selectivity properties similar to erlotinib against various types of EGFR. The results obtained after injecting 6-O-[$^{18}$F]FEE into NSCLC tumor-bearing mice show that this radiopharmaceutical is capable of distinguishing tumors harboring the WT receptor from those harboring an exon 19 deletion mutation or the double

L858R/T790M mutation, indicating that more clinical studies are needed to characterize the full potential of this compound for PET MI of the EGFR in NSCLC patients [34].

*2.12. [$^{11}$C]osimertinib*

The *ex vivo* biodistribution of methylindole-[$^{11}$C]osimertinib and dimethylamine-[$^{11}$C]osimertinib in female nu/nu mice carrying A549 tumors was examined at 5, 15, and 45 minutes post-injection. Both methylindole-[$^{11}$C]- and dimethylamine-[$^{11}$C]osimertinib showed rapid clearance of radioactivity in blood, with 1.23 ± 0.27%ID/g and 0.76 ± 0.10%ID/g accumulation after 45 minutes post-injection, respectively. Both tracers had a similar distribution pattern, as well as organ uptake and retention. Both tracers showed high uptake in the brain, with 5.94 ± 1.79%ID/g for methylindole-[$^{11}$C]osimertinib and 5.46 ± 2.53%ID/g for dimethylamine-[$^{11}$C]osimertinib at 5 minutes post injection [35].

At all-time points, high uptake was found in the kidneys and liver. At 45 minutes after injection, high uptake was also detected in the lungs (17.88 ± 1.45%ID/g for methylindole-[$^{11}$C]osimertinib and 27.42 ± 7.19%ID/g for dimethylamine- [$^{11}$C]osimertinib). The lungs may operate as slow-release mechanisms for both tracers after the initial high uptake, altering pharmacokinetics and explaining the increasing uptake in time in tumor, skin, and muscle organs expressing EGFR [26]. The high lung uptake may limit the clinical application of the PET tracers [35].

Both tracers enhanced tumor uptake over time, resulting in a statistically significant ($P$ = 0.0072) higher tumor uptake of 1.90 ± 0.27%ID/g for methylindole-[$^{11}$C]osimertinib at 45 minutes compared to 1.54 ± 0.19%ID/g for dimethylamine-[$^{11}$C]osimertinib. However, the T/B ratio was lower for methylindole-[$^{11}$C]osimertinib (1.58 ± 0.24 vs. 2.02 ± 0.16, $P$ = 0.0007), which is most likely due to the higher concentration in blood as a result of methylindole-[$^{11}$C]osimertinib release from the lungs, which is higher compared to dimethylamine-[$^{11}$C]osimertinib. The T/M ratio was considerably greater 45 minutes after methylindole-[$^{11}$C]osimertinib injection compared to dimethylamine-[$^{11}$C]osimertinib (1.17 ± 0.15 vs. 0.91 ± 0.16, $P$ = 0.0042), indicating that the release of methylindole-[$^{11}$C]osimertinib from the lungs had less influence [35].

HCC827 xenografted mice were subjected to two 45-minute dynamic PET scans with both tracers in the same animal, with a full day of rest in between. Both tracers demonstrated equivalent tumor uptake by PET/CT, as validated by an *ex vivo* biodistribution 45 minutes after injection. The T/M ratio was higher for methylindole-[$^{11}$C]osimertinib, similar to what was reported in A549 xenografted mice, whereas the T/B ratio was higher for dimethylamine-[$^{11}$C]Osimertinib [35].

Despite having a higher uptake in A549, methylindole-[$^{11}$C]osimertinib is somewhat favored as a tracer over dimethylamine-[$^{11}$C]osimertinib regarding absolute tumor uptake and T/M ratio. More notably, methylindole-[$^{11}$C]osimertinib demonstrated decreased lung uptake 45 minutes after injection, which is advantageous because the tracer would be utilized to assess lung cancers in a clinical context. Based on these findings, methylindole-[$^{11}$C]osimertinib was chosen for future testing [35].

PET/CT blocking tests with methylindole-[$^{11}$C]osimertinib were carried out in HCC827 xenografted. Following a 24-hour recovery time after establishing a baseline, the mice were given 15 mg/kg osimertinib an hour before the second PET/CT. There was no statistically significant difference between the time-activity curves. The selectivity of tumor uptake was assessed by pretreatment of the mice with afatinib. HCC827 xenografted mice were treated

with a baseline PET scan, followed by a 24-hour recovery period before administration with afatinib (15 mg/kg). The time-activity curves did not indicate a statistically significant difference after afatinib pretreatment [35].

Within 1 to 2 hours of incubation, methylindole-[$^{3}$H]osimertinib accumulation reached a plateau in all three cell lines. After that, methylindole-[3H]osimertinib retention was evaluated by removing and replacing the medium containing methylindole-[3H]osimertinib with a medium. When the uptake and retention patterns were compared, it was discovered that the negative control cell line, A549, maintained two-thirds of the radioactivity even after a medium change, indicating that a large fraction was bound or trapped in the cells. Because the A549 cell expresses WT EGFR, it is unknown why A549 cells retain methylindole-[$^{3}$H] osimertinib so well. However, the observed lack of selective absorption of both carbon-11 labeled tracers in vivo is most likely explained by the strong non-selective uptake of methylindole-[$^{3}$H]Osimertinib [35].

The EGFR PET tracers methylindole-[$^{11}$C]osimertinib and dimethylamine-[$^{11}$C]osimertinib were effectively tagged in two places using carbon-11. *Ex vivo* and in vivo investigations validated uptake and retention of activity in three NSCLC xenografts: A549 expressing WT EGFR, HCC827 expressing Del19 mutant EGFR, and H1975 expressing T790M mutated EGFR. Although methylindole-[$^{11}$C]osimertinib did not distinguish between H1975 and A549, it did distinguish between Del19 mutant EGFR expressing HCC827 and A549 based on T/M ratios [35].

## 3. Discussion

In this study, we have summarized some of the most noteworthy discoveries about small compounds created as radiotracers for imaging EGFR Del19 and L858R. Most of the studies in this evaluation assessed tracers based on their ability to distinguish tumors based on EGFR expression or mutational status. In several studies, some cell lines have been used for either purpose.

Several types of NSCLC cancer cell lines are used in the cellular uptake study, as shown in Table 1. The overexpression of EGFR differentiates each cell. For all the articles reviewed, just one cell, H3255, was employed to evaluate radiotracer accumulation toward EGFR L858R. Meanwhile, three cell lines were used to study EGFR Del19, namely H1650, PC9, and HCC827. Six cell lines expressing EGFR WT were used as a negative control. The different cell lines employed in each investigation make comprehensive accumulation comparisons challenging. As a result, we write down the existing cellular accumulation study findings in this review without comparing them.

Many studies have used blocking tests to demonstrate the tracer's specificity. Self-blocking has become a popular technique. However, this is an unfavorable method because self-blocking will not demonstrate affinity for another kinase because the cold chemical will also block these off-target receptors [36-38]. To decrease the chance of the chemical occupying the same off-target kinases, it is advisable to use a separate TKI to inhibit the EGFR.

Mice are commonly employed in preclinical testing of small molecule radiotracers [39,40]. A significant variation in radioactivity concentration was reported in the *ex vivo* biodistribution research between male ddY mice and female BALB/C nu/nu mice. It was not stated whether this was due to mouse strain or sex. Because sex can influence xenobiotics' pharmacokinetics, metabolism, and bioavailability, investigations must account for this [41-43].

## 4. Conclusions

Some radiolabeled imaging probes targeting EGFR Del19 and L858R active mutants were identified. These radiolabeled small molecules were created and fundamentally evaluated in vitro and in vivo. Compared to the wild-type, several radiolabeled probes accumulated preference toward EGFR Del19 and L858R. However, the summary report indicates that these probes must be structurally modified to increase imaging contrast for clinical research.

## Funding

This work was supported by the Ministry of Research, Technology and Higher Education through the LP2S Universitas Muslim Indonesia, with grant number 079/E5/PG.02.00.PL/2023; 440/L.L9/PK.00.PG/2023.

## Acknowledgments

The authors acknowledge the Faculty of Pharmacy and LP2S Universitas Muslim Indonesia for their support and encouragement in carrying out this research.

## Conflicts of Interest

The authors declare no conflict of interest.

## References

1. Siegel, R.L.; Miller, K.D.; Wagle, N.S.; Jemal, A. Cancer statistics, 2023. *CA: Cancer J. Clin.* **2023**, *73*, 17-48, https://doi.org/10.3322/caac.21763.
2. Zappa, C.; Mousa, S.A. Non-small cell lung cancer: current treatment and future advances. *Transl. Lung Cancer Res.* **2016**, *5*, 288-300, https://doi.org/10.21037%2Ftlcr.2016.06.07.
3. Lan, C.-C.; Hsieh, P.-C.; Huang, C.-Y.; Yang, M.-C.; Su, W.-L.; Wu, C.-W.; Wu, Y.-K. Review of epidermal growth factor receptor-tyrosine kinase inhibitors administration to non-small-cell lung cancer patients undergoing hemodialysis. *World J. Clin. Cases* **2022**, *10*, 6360-6369, https://doi.org/10.12998/wjcc.v10.i19.6360.
4. Kujtan, L.; Subramanian, J. Epidermal growth factor receptor tyrosine kinase inhibitors for the treatment of non-small cell lung cancer. *Expert Rev. Anticancer Ther.* **2019**, *19*, 547-559, https://doi.org/10.1080/14737140.2019.1596030.
5. Lopes, G.L.; Vattimo, E.F.d.Q.; Castro Junior, G.d. Identifying activating mutations in the EGFR gene: prognostic and therapeutic implications in non-small cell lung cancer. *J. Bras. Pneumol.* **2015**, *41*, 365-375, https://doi.org/10.1590/s1806-37132015000004531.
6. Iommelli, F.; De Rosa, V.; Fonti, R.; Del Vecchio, S. Molecular imaging for detection of sensitivity and resistance to EGFR tyrosine kinase inhibitors in non-small cell lung cancer. *Clin. Transl. Imaging* **2014**, *2*, 43-53, https://doi.org/10.1007/s40336-014-0050-6.
7. Shigematsu, H.; Lin, L.; Takahashi, T.; Nomura, M.; Suzuki, M.; Wistuba, I.I.; Fong, K.M.; Lee, H.; Toyooka, S.; Shimizu, N.; Fujisawa, T.; Feng, Z.; Roth, J.A.; Herz, J.; Minna, J.D.; Gazdar, A.F. Clinical and Biological Features Associated With Epidermal Growth Factor Receptor Gene Mutations in Lung Cancers. *J. Natl. Cancer Inst.* **2005**, *97*, 339-346, https://doi.org/10.1093/jnci/dji055.
8. Ochi, N.; Takeyama, M.; Miyake, N.; Fuchigami, M.; Yamane, H.; Fukazawa, T.; Nagasaki, Y.; Kawahara, T.; Nakanishi, H.; Takigawa, N. The complexity of EGFR exon 19 deletion and L858R mutant cells as assessed by proteomics, transcriptomics, and metabolomics. *Exp. Cell Res.* **2023**, *424*, 113503, https://doi.org/10.1016/j.yexcr.2023.113503.
9. Low, J.L.; Lim, S.M.; Lee, J.B.; Cho, B.C.; Soo, R.A. Advances in the management of non-small-cell lung cancer harbouring *EGFR* exon 20 insertion mutations. *Ther. Adv. Med. Oncol.* **2023**, *15*, 17588359221146131, https://doi.org/10.1177/17588359221146131.
10. Makino, A.; Miyazaki, A.; Tomoike, A.; Kimura, H.; Arimitsu, K.; Hirata, M.; Ohmomo, Y.; Nishii, R.; Okazawa, H.; Kiyono, Y.; Ono, M.; Saji, H. PET probe detecting non-small cell lung cancer susceptible to epidermal growth factor receptor tyrosine kinase inhibitor therapy. *Bioorg. Med. Chem.* **2018**, *26*, 1609-1613, https://doi.org/10.1016/j.bmc.2018.02.007.

11. Ogawa, K.; Takeda, T.; Yokokawa, M.; Yu, J.; Makino, A.; Kiyono, Y.; Shiba, K.; Kinuya, S.; Odani, A. Comparison of Radioiodine- or Radiobromine-Labeled RGD Peptides between Direct and Indirect Labeling Methods. *Chem. Pharm. Bull.* **2018**, *66*, 651-659, https://doi.org/10.1248/cpb.c18-00081.
12. Sun, X.; Cai, W.; Chen, X. Positron Emission Tomography Imaging Using Radiolabeled Inorganic Nanomaterials. *Acc. Chem. Res.* **2015**, *48*, 286-294, https://doi.org/10.1021/ar500362y.
13. Alati, S.; Singh, R.; Pomper, M.G.; Rowe, S.P.; Banerjee, S.R. Preclinical Development in Radiopharmaceutical Therapy for Prostate Cancer. *Semin. Nucl. Med.* **2023**, *53*, 663-686, https://doi.org/10.1053/j.semnuclmed.2023.06.007.
14. Xiao, Y.; Mei, C.; Xu, D.; Yang, F.; Yang, M.; Bi, L.; Mao, J.; Pang, P.; Li, D. Identification of a CEACAM5 targeted nanobody for positron emission tomography imaging and near-infrared fluorescence imaging of colorectal cancer. *Eur. J. Nucl. Med. Mol. Imaging* **2023**, *50*, 2305-2318, https://doi.org/10.1007/s00259-023-06183-7.
15. Decazes, P.; Bohn, P. Immunotherapy by Immune Checkpoint Inhibitors and Nuclear Medicine Imaging: Current and Future Applications. *Cancers* **2020**, *12*, 371, https://doi.org/10.3390/cancers12020371.
16. Fawwaz, M.; Mishiro, K.; Nishii, R.; Sawazaki, I.; Shiba, K.; Kinuya, S.; Ogawa, K. Synthesis and Fundamental Evaluation of Radioiodinated Rociletinib (CO-1686) as a Probe to Lung Cancer with L858R/T790M Mutations of Epidermal Growth Factor Receptor (EGFR). *Molecules* **2020**, *25*, 2914, https://doi.org/10.3390/molecules25122914.
17. Winuprasith, T.; Koirala, P.; McClements, D.J.; Khomein, P. Emulsion Technology in Nuclear Medicine: Targeted Radionuclide Therapies, Radiosensitizers, and Imaging Agents. *Int. J. Nanomed.* **2023**, *18*, 4449-4470, https://doi.org/10.2147/ijn.S416737.
18. Hashimoto, K.; Nishimura, S.; Ito, T.; Oka, N.; Akagi, M. Limitations and usefulness of biopsy techniques for the diagnosis of metastatic bone and soft tissue tumors. *Ann. Med. Surg.* **2021**, *68*, 102581, https://doi.org/10.1016/j.amsu.2021.102581.
19. Wilcox Vanden Berg, R.N.; George, A.K.; Kaye, D.R., Should Transperineal Prostate Biopsy Be the Standard of Care?. *Curr. Urol. Rep.* **2023**, *24*, 135-142, https://doi.org/10.1007/s11934-022-01139-0.
20. Yang, F.; Xiao, Y.; Ding, J.-H.; Jin, X.; Ma, D.; Li, D.-Q.; Shi, J.-X.; Huang, W.; Wang, Y.-P.; Jiang, Y.-Z.; Shao, Z.-M. Ferroptosis heterogeneity in triple-negative breast cancer reveals an innovative immunotherapy combination strategy. *Cell Metab.* **2023**, *35*, 84-100.e8, https://doi.org/10.1016/j.cmet.2022.09.021.
21. Yeh, H.H.; Ogawa, K.; Balatoni, J.; Mukhapadhyay, U.; Pal, A.; Gonzalez-Lepera, C.; Shavrin, A.; Soghomonyan, S.; Flores, L.; Young, D.; Volgin, A.Y.; Najjar, A.M.; Krasnykh, V.; Tong, W.; Alauddin, M.M.; Gelovani, J.G. Molecular imaging of active mutant L858R EGF receptor (EGFR) kinase-expressing non-small cell lung carcinomas using PET/CT. *Proc. Natl. Acad. Sci. U.S.A.* **2011**, *108*, 1603-1608, https://doi.org/10.1073/pnas.1010744108.
22. Casagrande, G.M.S.; Silva, M.d.O.; Reis, R.M.; Leal, L.F. Liquid Biopsy for Lung Cancer: Up-to-Date and Perspectives for Screening Programs. *Int. J. Mol. Sci.* **2023**, *24*, 2505, https://doi.org/10.3390/ijms24032505.
23. Shen, Y.; Yang, W.; Liu, J.; Zhang, Y. Minimally invasive approaches for the early detection of endometrial cancer. *Mol. Cancer* **2023**, *22*, 53, https://doi.org/10.1186/s12943-023-01757-3.
24. Fawwaz, M.; Pratama, M.; Aminuddin, A.H.; Baits, M. Radiolabeled EGFR Tyrosine Kinase for the Detection of Dual Mutations EGFR L858R/T790M in NSCLC. *Biointerface Res. Appl. Chem.* **2023**, *13*, 500, https://doi.org/10.33263/BRIAC135.500.
25. Fawwaz, M.; Mishiro, K.; Nishii, R.; Makino, A.; Kiyono, Y.; Shiba, K.; Kinuya, S.; Ogawa, K. A Radiobrominated Tyrosine Kinase Inhibitor for EGFR with L858R/T790M Mutations in Lung Carcinoma. *Pharmaceuticals* **2021**, *14*, 256, https://doi.org/10.3390/ph14030256.
26. Yeh, S.H.-H.; Lin, C.-F.; Kong, F.-L.; Wang, H.-E.; Hsieh, Y.-J.; Gelovani, J.G.; Liu, R.-S. Molecular imaging of non-small cell lung carcinomas expressing active mutant EGFR kinase using PET with [(124)i]-morpholino-IPQA. *Biomed. Res. Int.* **2013**, *2013*, 549359, https://doi.org/10.1155/2013/549359.
27. Yoshimoto, M.; Hirata, M.; Kanai, Y.; Naka, S.; Nishii, R.; Kagawa, S.; Kawai, K.; Ohmomo, Y. Monitoring of Gefitinib Sensitivity with Radioiodinated PHY Based on EGFR Expression. *Biol. Pharm. Bull.* **2014**, *37*, 355-360, https://doi.org/10.1248/bpb.b13-00559.
28. Slobbe, P.; Windhorst, A.D.; Stigter-van Walsum, M.; Smit, E.F.; Niessen, H.G.; Solca, F.; Stehle, G.; van Dongen, G.A.M.S.; Poot, A.J. A comparative PET imaging study with the reversible and irreversible EGFR tyrosine kinase inhibitors [$^{11}$C]erlotinib and [$^{18}$F]afatinib in lung cancer-bearing mice. *EJNMMI Res.* **2015**, *5*, 14, https://doi.org/10.1186/s13550-015-0088-0.
29. Dai, D.; Li, X.-F.; Wang, J.; Liu, J.-J.; Zhu, Y.-J.; Zhang, Y.; Wang, Q.; Xu, W.-G. Predictive efficacy of $^{11}$C-PD153035 PET imaging for EGFR-tyrosine kinase inhibitor sensitivity in non-small cell lung cancer patients. *Int. J. Cancer* **2016**, *138*, 1003-1012, https://doi.org/10.1002/ijc.29832.
30. Xiao, Z.; Song, Y.; Wang, K.; Sun, X.; Shen, B. One-step radiosynthesis of $^{18}$F-IRS: A novel radiotracer targeting mutant EGFR in NSCLC for PET/CT imaging. *Bioorg. Med. Chem. Lett.* **2016**, *26*, 5985-5988, https://doi.org/10.1016/j.bmcl.2016.10.084.

31. Xiao, Z.; Song, Y.; Kai, W.; Sun, X.; Shen, B. Evaluation of $^{99m}$Tc-HYNIC-MPG as a novel SPECT radiotracer to detect EGFR-activating mutations in NSCLC. *Oncotarget* **2017**, *8*, 40732-40740, https://doi.org/10.18632/oncotarget.17251.
32. Kimura, H.; Okuda, H.; Ishiguro, M.; Arimitsu, K.; Makino, A.; Nishii, R.; Miyazaki, A.; Yagi, Y.; Watanabe, H.; Kawasaki, I.; Ono, M.; Saji, H. $^{18}$F-Labeled Pyrido[3,4-*d*]pyrimidine as an Effective Probe for Imaging of L858R Mutant Epidermal Growth Factor Receptor. *ACS Med. Chem. Lett.* **2017**, *8*, 418-422, https://doi.org/10.1021/acsmedchemlett.6b00520.
33. Sun, X.; Xiao, Z.; Chen, G.; Han, Z.; Liu, Y.; Zhang, C.; Sun, Y.; Song, Y.; Wang, K.; Fang, F.; Wang, X.; Lin, Y.; Xu, L.; Shao, L.; Li, J.; Cheng, Z.; Gambhir, S.S.; Shen, B. A PET imaging approach for determining EGFR mutation status for improved lung cancer patient management. *Sci. Transl. Med.* **2018**, *10*, eaan8840, https://doi.org/10.1126/scitranslmed.aan8840.
34. Shamni, O.; Grievink, H.; Itamar, B.; Mishani, E.; Abourbeh, G. Development of a Fluorinated Analogue of Erlotinib for PET Imaging of EGFR Mutation-Positive NSCLC. *Mol. Imaging Biol.* **2019**, *21*, 696-704, https://doi.org/10.1007/s11307-018-1286-8.
35. Högnäsbacka, A.; Poot, A.J.; Kooijman, E.; Schuit, R.C.; Schreurs, M.; Verlaan, M.; van den Hoek, J.; Heideman, D.A.M.; Beaino, W.; van Dongen, G.A.M.S.; Vugts, D.J.; Windhorst, A.D. Synthesis and preclinical evaluation of two osimertinib isotopologues labeled with carbon-11 as PET tracers targeting the tyrosine kinase domain of the epidermal growth factor receptor. *Nucl. Med. Biol.* **2023**, *120-121*, 108349, https://doi.org/10.1016/j.nucmedbio.2023.108349.
36. Högnäsbacka, A.; Poot, A.J.; Vugts, D.J.; van Dongen, G.A.M.S.; Windhorst, A.D. The Development of Positron Emission Tomography Tracers for In Vivo Targeting the Kinase Domain of the Epidermal Growth Factor Receptor. *Pharmaceuticals* **2022**, *15*, 450, https://doi.org/10.3390/ph15040450.
37. Zhao, L.; Wen, X.; Xu, W.; Pang, Y.; Sun, L.; Wu, X.; Xu, P.; Zhang, J.; Guo, Z.; Lin, Q.; Chen, X.; Chen, H. Clinical Evaluation of $^{68}$Ga-FAPI-RGD for Imaging of Fibroblast Activation Protein and Integrin $\alpha_v\beta_3$ in Various Cancer Types. *J. Nucl. Med.* **2023**, *64*, 1210-1217, https://doi.org/10.2967/jnumed.122.265383.
38. Qin, X.; Guo, X.; Liu, T.; Li, L.; Zhou, N.; Ma, X.; Meng, X.; Liu, J.; Zhu, H.; Jia, B.; Yang, Z. High in-vivo stability in preclinical and first-in-human experiments with [$^{18}$F]AlF-RESCA-MIRC213: a $^{18}$F-labeled nanobody as PET radiotracer for diagnosis of HER2-positive cancers. *Eur. J. Nucl. Med. Mol. Imaging* **2023**, *50*, 302-313, https://doi.org/10.1007/s00259-022-05967-7.
39. Chen, Y.-J.; Liao, P.-X.; Kuo, W.-H.; Chen, C.-Y.; Ding, S.-T.; Wang, M.-H. Assessment of Brown and Beige Adipose Tissue Activation in Mice Using PET/CT Imaging. In Thermogenic Fat. Methods in Molecular Biology; Lodhi, I.J., Ed.; Humana, New York, NY, **2023**; Volume 2662, 135-145, https://doi.org/10.1007/978-1-0716-3167-6_12.
40. Shan, H.-M.; Maurer, M.A.; Schwab, M.E. Four-parameter analysis in modified Rotarod test for detecting minor motor deficits in mice. *BMC Biol.* **2023**, *21*, 177, https://doi.org/10.1186/s12915-023-01679-y.
41. Hildebrandt, I.J.; Su, H.; Weber, W.A. Anesthesia and Other Considerations for in Vivo Imaging of Small Animals. *ILAR J.* **2008**, *49*, 17-26, https://doi.org/10.1093/ilar.49.1.17.
42. Doyle, M.R.; Martinez, A.R.; Qiao, R.; Dirik, S.; Di Ottavio, F.; Pascasio, G.; Martin-Fardon, R.; Benner, C.; George, O.; Telese, F.; de Guglielmo, G. Strain and sex-related behavioral variability of oxycodone dependence in rats. *Neuropharmacology* **2023**, *237*, 109635, https://doi.org/10.1016/j.neuropharm.2023.109635.
43. Torrens, A.; Roy, P.; Lin, L.; Vu, C.; Grimes, D.; Inshishian, V.C.; Montesinos, J.S.; Ahmed, F.; Mahler, S.V.; Huestis, M.A.; Das, A.; Piomelli, D. Comparative Pharmacokinetics of $\Delta^9$-Tetrahydrocannabinol in Adolescent and Adult Male and Female Rats. *Cannabis Cannabinoid Res.* **2022**, *7*, 814-826, https://doi.org/10.1089/can.2021.0205.